

Effect of collective spin excitations on electronic transport in topological spin texturesKohei Hattori,^{1,*} Hikaru Watanabe^{2,†}, Junta Iguchi,¹ Takuya Nomoto^{2,3} and Ryotaro Arita^{2,4}¹*Department of Applied Physics, The University of Tokyo, Bunkyo, Tokyo 113-8656, Japan*²*Research Center for Advanced Science and Technology, The University of Tokyo, Meguro, Tokyo 153-8904, Japan*³*Department of Physics, Tokyo Metropolitan University, Hachioji, Tokyo 192-0397, Japan*⁴*Center for Emergent Matter Science, RIKEN, Wako, Saitama 351-0198, Japan*

(Received 8 April 2024; accepted 21 June 2024; published 16 July 2024)

We develop an efficient real-time simulation method for the spin-charge coupled system in the velocity gauge. This method enables us to compute the real-time simulation for the two-dimensional system with a complex spin texture. We focus on the effect of the collective excitation of the localized spins on the electronic transport properties of the nontrivial topological state in real space. To investigate this effect, we calculate the linear optical conductivity by calculating the real-time evolution of the Kondo lattice model on the triangular lattice, which hosts an all-in/all-out (triple- Q) magnetic structure. In the linear conductivity spectra, we observe multiple peaks below the band gap regime, attributed to the resonant contributions of collective modes similar to the skyrmionic system, alongside broadband modifications resulting from off-resonant spin dynamics. This result shows that the collective excitation, similar to the skyrmionic system, influences the optical response of the electron systems based on symmetry analysis. We elucidate the interference between the contributions from the different spin excitations to the optical conductivity in the multiple-spin texture, pointing out the mode-dependent electrical activity. We show the complex interplay between the complex spin texture and the itinerant electrons in the two-dimensional spin-charge coupled system.

DOI: [10.1103/PhysRevB.110.014425](https://doi.org/10.1103/PhysRevB.110.014425)**I. INTRODUCTION**

Recent research intensively elucidated the effect of the collective dynamics of a spontaneous order, such as magnetic order and excitonic order, on the optical responses of electronic systems [1–7]. For instance, theoretical studies simultaneously calculated the real-time evolution of the electron system and the order parameter [4–7]. More specifically, the study of magnetic order [4] showed that the collective excitation of the localized spins modulates the linear optical conductivity and photocurrent response in an antiferromagnetic chain. The results identified the features which are absent within the independent particle approximation. It is, however, not straightforward to apply the methodology to more complex systems, such as two-dimensional systems with a complex spin structure, due to their large computational cost. The realization of efficient real-time simulation applicable to diverse cases is highly desirable since it is anticipated that one can explore intriguing spin-charge coupled dynamics, for example, by considering a magnetic order whose real-space topological texture may significantly influence electronic properties [8–11].

The nontrivial topological state in real space appears in noncoplanar magnetic structures such as frustrated magnets and magnetic skyrmionic systems, where the complex spin texture forms by spin-orbit coupling [12] and itinerant-

electron-mediated interactions [13,14]. Through the exchange interaction with localized spin systems with such nontrivial spin textures, the electron system feels the fictitious magnetic field and exhibits anomalous transverse transport. Theoretical studies [8,9,15–19] showed that the anomalous transverse conduction occurs in the Kondo lattice model with nontrivial spin structures. Importantly, such noncoplanar spin textures, including the all-in/all-out (AIAO) structure (triple- Q structure) [20–22] and skyrmion crystal [13,14,23], allow for collective modes richer than those in conventional ferro- and antiferromagnets. Indeed, theoretical [24–26] and experimental studies [27–29] identified collective modes of the localized spins in the skyrmionic system. These collective modes include breathing modes excited by out-of-plane magnetic fields and clockwise and counterclockwise rotatory modes excited by in-plane magnetic fields [24,25].

In this study, we elaborate on the effect of the collective excitation of the AIAO spin texture on the anomalous transverse transport of the electron system. We simulate the real-time evolution of the Kondo lattice model on the triangular lattice hosting an AIAO spin texture composed of four sites in the unit cell. The dynamical property is clarified by computing the real-time evolution of the electrons and localized spins simultaneously. The computational cost of the two-dimensional spin-charge coupled system with the AIAO spin texture is expensive because of the dimensionality and complex spin structure. We resolve the difficulty by developing an efficient real-time simulation based on the velocity-gauge formulation and interpolation technique. The developed calculation scheme allows us to demonstrate the intriguing interplay

*Contact author: hattori-kohei053@g.ecc.u-tokyo.ac.jp

†Contact author: hikaru-watanabe@g.ecc.u-tokyo.ac.jp

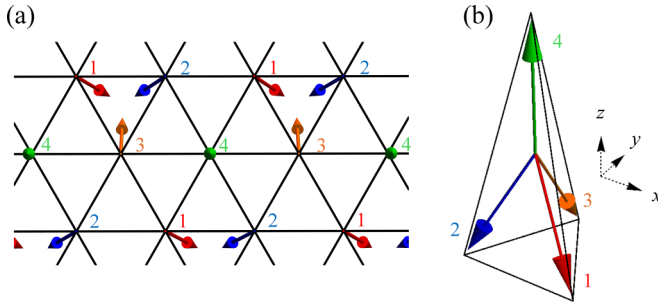


FIG. 1. (a) Kondo lattice model with AIAO order on a triangular lattice with a four-sublattice unit cell. (b) Spin moments of each sublattice. The spin texture is an AIAO state including a canted component along the z axis.

between the complex spin texture and itinerant electrons in a two-dimensional system.

The real-time simulation unambiguously shows that the optical conductivity spectrum of the electron system exhibits multiple peaks originating from rich collective dynamics of localized spins. To classify which collective mode affects linear optical conductivity, we analyze the spin excitations using the symmetry-adapted bases. The symmetry analysis indicates the similarity between the collective modes of the AIAO spin system and those of the skyrmionic system. We find that the rotatory modes of the localized spins affect the optical responses of the electronic systems in two-dimensional systems. Furthermore, the interference effect of the collective modes, which is characteristic of a system hosting a complex spin structure, results in an in-gap spectrum of the optical Hall conductivity whose intensity significantly differs between the modes. These findings may lead to an understanding of the interplay between the complex spin texture and itinerant electrons.

This paper is organized as follows. In Sec. II, we explain the details of the model and the computational scheme for the real-time evolution of the spin-charge coupled system. Section III discusses the symmetry classification of the spin excitations and its coupling to the external stimuli. Then, we elucidate the physical responses and corroborate the effects of the spin-charge coupled dynamics in Sec. IV. We draw our conclusions in Sec. V.

II. METHOD

A. Model

We work with a AIAO state in the Kondo lattice model on a triangular lattice (Fig. 1). The tight-binding Hamiltonian is expressed as

$$\hat{\mathcal{H}} = - \sum_{\langle ij \rangle \sigma \sigma'} t_h \hat{c}_{i\sigma}^\dagger \hat{c}_{j\sigma'} - J \sum_{i\sigma\sigma'} \hat{c}_{i\sigma}^\dagger \mathbf{S}_i \cdot \boldsymbol{\sigma}_{\sigma\sigma'} \hat{c}_{i\sigma'} - i\lambda \sum_{\langle ij \rangle \sigma \sigma'} \hat{c}_{i\sigma}^\dagger \mathbf{e}_{ij} \cdot \boldsymbol{\sigma}_{\sigma\sigma'} \hat{c}_{j\sigma'} - K_z \sum_i (S_i^z)^2. \quad (1)$$

$\hat{c}_{i\sigma}^\dagger$ ($\hat{c}_{i\sigma}$) is the creation (annihilation) operator of the electron on site i with spin index σ ($\sigma = \uparrow, \downarrow$). The first term of the Hamiltonian represents the hopping of the electrons between the nearest-neighbor sites $\langle ij \rangle$ with amplitude t_h . The second

term represents the exchange interaction J between the spin moment $\boldsymbol{\sigma}$ of the itinerant electron and the localized spin moment \mathbf{S} . The third term represents the antisymmetric spin-orbit coupling λ (ASOC), which acts as an effective magnetic field parallel to the vector \mathbf{e}_{ij} between the nearest-neighbor sites $\langle ij \rangle$. The ASOC breaks the inversion symmetry and thereby allows the system to exhibit cross correlation between the spin and charge degrees of freedom. The last term represents the easy anisotropy of the localized spin system K_z .

In the following calculations we use the parameters $t_h = 1$, $J = 3.0$, $\lambda = 0.3$, $K_z = 0.1$, $\alpha_G = 0.01$, and $\gamma = 0.01$, unless explicitly stated otherwise. The filling number n of the electrons is set to 0.25 per unit cell to stabilize the AIAO state in equilibrium [Fig. 1(b)] [15,30], where the system shows insulating behavior. The AIAO spin texture is stabilized by the higher-order interaction between the local spins, which is included in the exchange coupling between the itinerant electrons and the local spins [31]. Owing to the anisotropy of the spin Hamiltonian, a finite magnetization appears along the z axis. We also set the lattice constant $a = 1$ and elementary charge $e = 1$.

We transform the Hamiltonian $\hat{\mathcal{H}}$ in the real-space representation into the momentum representation through the Fourier transformation

$$\hat{c}_{a\sigma}^\dagger(\mathbf{k}) = \sum_{\mathbf{R}} e^{i\mathbf{k} \cdot (\mathbf{r}_a + \mathbf{R})} \hat{c}_{a\sigma}^\dagger, \quad (2)$$

where the translation vectors \mathbf{R} are defined as $\mathbf{R} = n_1(2, 0, 0) + n_2(1, \sqrt{3}, 0)$ ($n_1, n_2 \in \mathbb{Z}$) and the position $\mathbf{r}_{a'}$ of the lattice site a' is $\mathbf{r}_{a'} = \mathbf{r}_a + \mathbf{R}$. Since the AIAO state has a unit cell 4 times larger than that in the paramagnetic state, the index a for the sublattice in $\hat{c}_{a\sigma}^\dagger(\mathbf{k})$ is taken as $a = 1, 2, 3, 4$ [Fig. 1(a)]. The Hamiltonian $\hat{\mathcal{H}}$ in the momentum representation reads

$$\hat{\mathcal{H}} = \sum_{\mathbf{k}} \sum_{\sigma\sigma'} \sum_{ab} [\mathcal{H}_0(\mathbf{k})]_{ab}^{\sigma\sigma'} \hat{c}_{a\sigma}^\dagger(\mathbf{k}) \hat{c}_{b\sigma'}(\mathbf{k}), \quad (3)$$

where $\mathcal{H}_0(\mathbf{k})$ is the electronic Hamiltonian at each \mathbf{k} point.

When the electric field is incorporated under the velocity gauge, the creation (annihilation) operator changes as $\hat{c}_{i\sigma}^\dagger \rightarrow e^{i\mathbf{A}(t) \cdot \mathbf{r}} \hat{c}_{i\sigma}^\dagger$ ($\hat{c}_{i\sigma} \rightarrow e^{-i\mathbf{A}(t) \cdot \mathbf{r}} \hat{c}_{i\sigma}$), where $\mathbf{A}(t)$ is the vector potential of the electromagnetic field. In the velocity gauge, a time-dependent Hamiltonian is

$$\hat{\mathcal{H}}(t) = \sum_{\mathbf{k}} \sum_{\sigma\sigma'} \sum_{ab} [\mathcal{H}(\mathbf{k}, t)]_{ab}^{\sigma\sigma'} \hat{c}_{a\sigma}^\dagger(\mathbf{k}) \hat{c}_{b\sigma'}(\mathbf{k}), \quad (4)$$

where the time-dependent electronic Hamiltonian $\mathcal{H}(\mathbf{k}, t)$ at each \mathbf{k} point is expressed as

$$\mathcal{H}(\mathbf{k}, t) = \mathcal{H}_0[\mathbf{k} - \mathbf{A}(t)], \quad (5)$$

while the creation and annihilation operators are coincident with the original operators in Eq. (3) without the dependence on t . The light-matter coupling is given by the time-dependent vector potential $\mathbf{A}(t)$ in the velocity gauge, which indicates the photoelectric field $\mathbf{E}(t) = -\partial_t \mathbf{A}(t)$. Since the light-matter coupling is taken into account with the electric dipole approximation, the vector potential is spatially uniform and thus does not break the translation symmetry. In Eq. (4), we assume that the Wannier state of an electron is well localized at a given site.

B. Calculation scheme

In this study, we calculate the real-time evolution of the spin-charge coupled system. To compute the real-time simulation, we simultaneously solve the von Neumann equation and the Landau-Lifshitz-Gilbert (LLG) equation.

First, the time evolution of electrons can be described by the single-particle density matrix (SPDM) $\rho_{ab}^{\sigma\sigma'}(\mathbf{k}, t) = \langle \hat{c}_{b\sigma'}^\dagger(\mathbf{k}) \hat{c}_{a\sigma}(\mathbf{k}) \rangle_t \equiv \text{Tr}[\hat{c}_{b\sigma'}^\dagger(\mathbf{k}) \hat{c}_{a\sigma}(\mathbf{k}) \hat{\rho}(t)]$, where $\hat{\rho}(t)$ is the density matrix of the system at time t . The SPDM satisfies the following equation, which is called the von Neumann equation [32]:

$$\frac{\partial \rho(\mathbf{k}, t)}{\partial t} = -i[\mathcal{H}(\mathbf{k}, t), \rho(\mathbf{k}, t)] - \gamma[\rho(\mathbf{k}, t) - \rho_{\text{eq}}(\mathbf{k}, t)]. \quad (6)$$

The vector potential $\mathbf{A}(t)$ for the light field does not break the translation symmetry, which keeps the von Neumann equation block diagonal with respect to the momentum \mathbf{k} . The \mathbf{k} -local property, which is compatible with the parallel computation, is advantageous for efficient simulation of the real-time evolution of spin-charge coupled dynamics. On the other hand, if one works on the length gauge under which the light field is expressed by the scalar potential as the Hamiltonian $-\mathbf{E}(t) \cdot \mathbf{r}$, the translation-symmetry breaking leads to the \mathbf{k} derivative of the SPDM $-\mathbf{E} \cdot \frac{\partial \rho(\mathbf{k}, t)}{\partial \mathbf{k}}$ in the von Neumann equation. This \mathbf{k} -derivative term is unfavorable for parallel computation of \mathbf{k} -point grids.

Second, the time evolution of the localized spin system is governed by the LLG equation

$$\frac{d\mathbf{S}_a}{dt} = \frac{1}{1 + \alpha_G^2} [\mathbf{H}_a^{\text{eff}} \times \mathbf{S}_a + \alpha_G \mathbf{S}_a \times (\mathbf{S}_a \times \mathbf{H}_a^{\text{eff}})], \quad (7)$$

$$\mathbf{H}_a^{\text{eff}} = -J(\boldsymbol{\sigma}_a) - 2K_z(0, 0, S_a^z). \quad (8)$$

Here, \mathbf{S}_a represents the localized spin moment at sublattice site a , and $\mathbf{H}_a^{\text{eff}}$ represents the effective magnetic field coupled to \mathbf{S}_a . In the LLG equation (7), $\langle \boldsymbol{\sigma}_a \rangle$ is the sublattice-dependent spin density of electrons calculated with SPDM [see Eq. (13)]. Furthermore, we account for a relaxation effect to obtain a physically reasonable response to light. Although relaxation stems from electron-electron correlations, electron-phonon interactions, and impurity scattering, we treat it phenomenologically by using the relaxation time approximation in the von Neumann equation $\gamma[\rho(\mathbf{k}, t) - \rho_{\text{eq}}(\mathbf{k}, t)]$ in Eq. (6) and the Gilbert damping α_G in Eq. (7). $\rho_{\text{eq}}(\mathbf{k}, t)$ is the SPDM in equilibrium at temperature $T = 0$. $\rho_{\text{eq}}(\mathbf{k}, t)$ represents an equilibrium property but shows dependence on time t when the light field is incorporated under the velocity gauge [33,34] (as discussed below). We solve the coupled equations (6) and (7) using the fourth-order Runge-Kutta method.

In the velocity gauge, the time-dependent Hamiltonian indicates modification of the velocity operator. The correction effectively gives rise to the shift in momentum \mathbf{k} , and thus, the momentum-resolved SPDM in equilibrium differs from that at initial time $t = 0$ by the momentum shift. The momentum shift explicitly reads

$$\rho_{\text{eq}}(\mathbf{k}, t) = \rho_{\text{eq}}^0[\mathbf{k} - \mathbf{A}(t)], \quad (9)$$

where $\rho_{\text{eq}}^0(\mathbf{k})$ is the SPDM of the initial Hamiltonian $\mathcal{H}_0(\mathbf{k})$. The SPDM of the equilibrium state $\tilde{\rho}_{\text{eq}}(\mathbf{k}, t)$ at time t is calculated in the Bloch basis as follows:

$$[\tilde{\rho}_{\text{eq}}(\mathbf{k}, t)]_{mn} = \delta_{mn} \Theta[\mu - \epsilon_n(\mathbf{k}, t)]. \quad (10)$$

We can compute the SPDM for the equilibrium state in the orbital basis by using the unitary transformation

$$\rho_{\text{eq}}(\mathbf{k}, t) = U(\mathbf{k}, t) \tilde{\rho}_{\text{eq}}(\mathbf{k}, t) U^\dagger(\mathbf{k}, t), \quad (11)$$

where the unitary matrix $U(\mathbf{k}, t)$ diagonalizes the Hamiltonian $\mathcal{H}(\mathbf{k}, t)$ as $U^\dagger(\mathbf{k}, t) \mathcal{H}(\mathbf{k}, t) U(\mathbf{k}, t) = \mathcal{E}(\mathbf{k}, t)$ and $[\mathcal{E}(\mathbf{k}, t)]_{mn} = \delta_{mn} \epsilon_n(\mathbf{k}, t)$. The Hamiltonian changes as $\mathcal{H}(\mathbf{k}, t) = \mathcal{H}_0[\mathbf{k} - \mathbf{A}(t)]$ due to the electric field. Therefore, we need to calculate the SPDM $\rho_{\text{eq}}(\mathbf{k}, t)$ at every time step by diagonalizing the Hamiltonian $\mathcal{H}(\mathbf{k}, t)$.

To avoid this large computational cost, we approximate the time-dependent SPDM in equilibrium. We calculate the SPDM $\rho_{\text{eq}}(\mathbf{k}, t)$ by applying cubic interpolation of the momentum grid. We initially calculate the SPDM $\rho_{\text{eq}}^0(\mathbf{k})$ at $t = 0$ and obtain the interpolated function $\rho_{\text{eq}}^{\text{int}}(\mathbf{k})$ by performing the cubic interpolation of $\rho_{\text{eq}}^0(\mathbf{k})$ with respect to \mathbf{k} . Then we can approximate the SPDM $\rho_{\text{eq}}(\mathbf{k}, t)$ at time t as

$$\rho_{\text{eq}}(\mathbf{k}, t) \simeq \rho_{\text{eq}}^{\text{int}}[\mathbf{k} - \mathbf{A}(t)]. \quad (12)$$

With this interpolation technique, we can calculate $\rho_{\text{eq}}(\mathbf{k}, t)$ easily without diagonalization of the Hamiltonian $\mathcal{H}(\mathbf{k}, t)$ at each time step.

Next, we explain a calculation method for physical responses. At each time step, we evaluate the physical quantity $\langle \hat{\mathcal{O}}(t) \rangle$ as

$$\langle \hat{\mathcal{O}}(t) \rangle = \frac{1}{N} \sum_{\mathbf{k}} \text{Tr}[\rho(\mathbf{k}, t) \mathcal{O}(\mathbf{k}, t)] \quad (13)$$

by using the SPDM. The current density operator is written as

$$\begin{aligned} \hat{j}(t) &= \frac{1}{n_{\text{sub}}} \sum_{\mathbf{k}} \sum_{ab} \sum_{\sigma\sigma'} \frac{\partial [\mathcal{H}(\mathbf{k}, t)]_{ab}^{\sigma\sigma'}}{\partial \mathbf{k}} \hat{c}_{a\sigma}^\dagger(\mathbf{k}) \hat{c}_{b\sigma'}(\mathbf{k}) \\ &\equiv \frac{1}{n_{\text{sub}}} \sum_{\mathbf{k}} \sum_{ab} \sum_{\sigma\sigma'} [\mathbf{j}(\mathbf{k}, t)]_{ab}^{\sigma\sigma'} \hat{c}_{a\sigma}^\dagger(\mathbf{k}) \hat{c}_{b\sigma'}(\mathbf{k}), \end{aligned} \quad (14)$$

where n_{sub} represents the number of sublattices in a unit cell. Then, the linear response function is obtained as follows. We apply an external field with a Gaussian profile described as

$$\mathbf{F}(t) = \frac{\mathbf{F}_0}{\sqrt{2\pi\sigma^2}} \exp\left(-\frac{(t-t_0)^2}{2\sigma^2}\right). \quad (15)$$

Since we take the velocity gauge for which $\mathbf{E}(t) = -\frac{\partial \mathbf{A}(t)}{\partial t}$ holds, the Gaussian electric field $\mathbf{E}(t)$ is incorporated by the vector potential $\mathbf{A}(t)$ given by

$$\mathbf{A}(t) = \frac{\mathbf{E}_0}{2} \left[\text{erf}\left(-\frac{t_0}{\sqrt{2}\sigma}\right) - \text{erf}\left(\frac{t-t_0}{\sqrt{2}\sigma}\right) \right], \quad (16)$$

with $\text{erf}(\cdot)$ being the error function. In this scheme, we can calculate the linear response function $\chi_{\mathcal{O}F}(\omega)$ of the physical quantity $\mathcal{O}(t)$ to the external field $\mathbf{F}(t)$ by the Fourier

TABLE I. Eigenvalues of symmetry-adapted bases of localized spins under a symmetry operation in magnetic point group \mathcal{G} . The subscript— in the ψ_α column represents the clockwise (CW) rotation, and the index+ represents the counterclockwise (CCW) rotation. In the 3_z and θ_{2_x} columns, +1 means the basis does not change sign, while -1 means that the sign of the operation flips. $\xi^- = \exp(2\pi i/3)$ denotes the eigenvalue of the CW mode, and $\xi^+ = \exp(-2\pi i/3)$ is that of the CCW mode. Each basis function ψ_α is explicitly written in the last column.

ψ_α	3_z	θ_{2_x}	Basis function
A_1^{1z}	+1	+1	S_4^z
A_1^{3z}	+1	+1	$\frac{1}{\sqrt{3}}(S_1^z + S_2^z + S_3^z)$
A_1^{3xy}	+1	+1	$\frac{1}{\sqrt{3}}[(\frac{\sqrt{3}}{2}S_1^x - \frac{1}{2}S_1^y) + (-\frac{\sqrt{3}}{2}S_2^x - \frac{1}{2}S_2^y) + S_3^y]$
A_2^{3xy}	+1	-1	$\frac{1}{\sqrt{3}}[(-\frac{1}{2}S_1^x - \frac{\sqrt{3}}{2}S_1^y) + (-\frac{1}{2}S_2^x + \frac{\sqrt{3}}{2}S_2^y) + S_3^x]$
E_\pm^{1xy}	ξ^\pm	-1	$\frac{1}{\sqrt{2}}(S_4^x \pm iS_4^y)$
E_\pm^{3z}	ξ^\pm	+1	$\frac{1}{\sqrt{2}}[(-\frac{1}{\sqrt{6}}S_1^z - \frac{1}{\sqrt{6}}S_2^z + \frac{2}{\sqrt{6}}S_3^z) \pm i(-\frac{1}{\sqrt{2}}S_1^x + \frac{1}{\sqrt{2}}S_2^x)]$
E_\pm^{3xy}	ξ^\pm	+1	$\frac{1}{\sqrt{2}}[\frac{1}{\sqrt{3}}\{(-\frac{\sqrt{3}}{2}S_1^x - \frac{1}{2}S_1^y) + (\frac{\sqrt{3}}{2}S_2^x - \frac{1}{2}S_2^y) + S_3^y\} \pm \frac{i}{\sqrt{3}}\{(-\frac{1}{2}S_1^x + \frac{\sqrt{3}}{2}S_1^y) + (-\frac{1}{2}S_2^x - \frac{\sqrt{3}}{2}S_2^y) + S_3^x\}]$
$E_\pm^{3xy'}$	ξ^\pm	-1	$\frac{1}{\sqrt{2}}[\frac{1}{\sqrt{3}}(S_1^x + S_2^x + S_3^x) \pm \frac{i}{\sqrt{3}}(S_1^y + S_2^y + S_3^y)]$

transformation

$$\chi_{\mathcal{O}F}(\omega) = \frac{\Delta\mathcal{O}(\omega)}{F(\omega)} = \frac{1}{F_0} e^{\frac{\sigma^2\omega^2}{2}} e^{i\omega t_0} \int_0^\infty \mathcal{O}(t) e^{-i\omega t} dt, \quad (17)$$

where $\Delta\mathcal{O}(\omega)$ is the Fourier component of $\Delta\mathcal{O}(t) = \mathcal{O}(t) - \mathcal{O}(0)$ and $F(\omega)$ is the Fourier component of the external field $F(t) = \frac{F_0}{\sqrt{2\pi\sigma^2}} \exp(-\frac{(t-t_0)^2}{2\sigma^2})$. In this calculation, we use the component of the external field $F_0 = 1.0 \times 10^{-5}$, $t_0 = 0.2$, and $\sigma = 0.03$. Based on this scheme, we calculate the linear response functions for the light field, which will be shown in the next section.

We set the k mesh of the Brillouin zone to 512×512 for the real-time simulation and to 1600×1600 for the cubic interpolation of the SPDM in equilibrium. In this calculation, we implement parallel computation of the k mesh using the message-passing interface.

III. SYMMETRY ANALYSIS

In this section, we present the symmetry analysis of the localized spin system. First, we classify the collective modes of the localized spins. Second, we analyze the collective spin dynamics that are linearly coupled to the external field based on the symmetry analysis.

A. Symmetry-adapted basis of localized spins

In this section, we analyze the collective modes of the localized spins in the framework of the magnetic representation and decompose them into three modes: the azimuthal symmetric (AS) mode, clockwise (CW) mode, and counterclockwise (CCW) mode.

The system belongs to the magnetic point group $\mathcal{G} = 32'$ and has the following symmetry:

$$\mathcal{G} = \{1, 3_z, 3_z^{-1}, \theta_{2_x}, \theta_{2_u}, \theta_{2_v}\}. \quad (18)$$

Here, 1, θ , 3_a , and 2_a are the identity operator, time-reversal operator, threefold rotation around the a axis, and twofold rotation around the a axis, respectively. The u and v axes are generated by the actions 3_z and 3_z^{-1} on the x axis, respectively. The representation Γ is obtained for the basis spanned by

the degrees of freedom of localized spin vectors S_a^μ . The dimension of Γ is 12 due to the sublattice ($a = 1, 2, 3, 4$) and spins ($\mu = x, y, z$). The representation is decomposed into irreducible representations as

$$\Gamma = 3A_1 \oplus A_2 \oplus 4E.$$

There are three symmetry-adapted bases for the irreducible representation A_1 , one for A_2 , and eight for E .

We further classify the symmetry-adapted modes by using threefold rotations. We define the AS mode as the mode with an eigenvalue of 1 under symmetry operation 3_z , the CW mode as that with $\xi^- = \exp(2\pi i/3)$, and the CCW mode as that with $\xi^+ = \exp(-2\pi i/3)$. The symmetry-adapted basis function is given by a linear combination of the localized spins S_a^μ as

$$\psi_\alpha = \sum_{a\mu} c_a^\mu(\alpha) S_a^\mu, \quad (19)$$

where $c_a^\mu(\alpha)$ is the coefficient of the symmetry-adapted basis ψ_α .

The dynamics of the localized spin system can be described by the symmetry-adapted basis listed in Table I. We display a sketch of the symmetry-adapted basis functions $\{\psi_\alpha\}$ in Fig. 2. The AS bases, A_1^{1z} , A_1^{3z} , A_1^{3xy} , and A_2^{3xy} , are invariant under the out-of-plane rotation and thus are totally symmetric in the azimuthal plane. The modes for clockwise rotation include E_-^{1xy} , E_-^{3z} , E_-^{3xy} , and $E_-^{3xy'}$, while the CCW mode comprises E_+^{1xy} , E_+^{3z} , E_+^{3xy} , and $E_+^{3xy'}$. Thus, CW and CCW modes have the nontrivial transformation property under the out-of-plane rotation. Note that the CCW basis with $\xi_+ = \exp(-2\pi i/3)$ is the complex conjugate of the CCW counterpart with $\xi_- = \exp(2\pi i/3)$. For example, E_+^{1xy} is the complex conjugate of E_-^{1xy} . These collective modes are similar to those of the skyrmionic system [24,25].

In the following sections, we calculate the component of the symmetry-adapted basis of the localized spin dynamics $\tilde{\psi}_\alpha(t)$ as

$$\tilde{\psi}_\alpha(t) = \sum_{a\mu} [c_a^\mu(\alpha)]^* S_a^\mu(t), \quad (20)$$

where we project the localized spins $S_a^\mu(t)$ into the symmetry-adapted basis ψ_α .

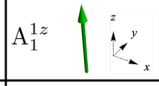
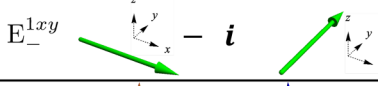
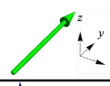
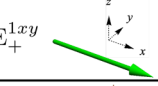
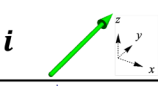
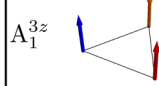
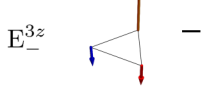
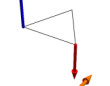
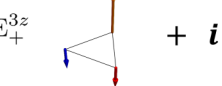
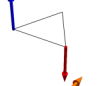
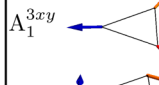
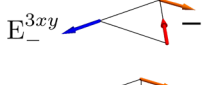
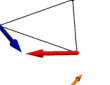
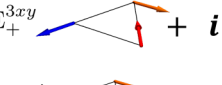

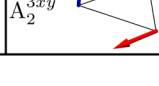
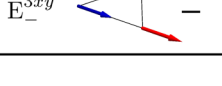
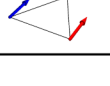
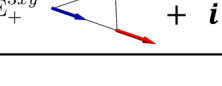
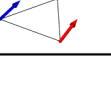
	AS	CW	CCW
Site 4	A_1^{1z} 	E_-^{1xy}  $-i$ 	E_+^{1xy}  $+i$ 
Site 1	A_1^{3z} 	E_-^{3z}  $-i$ 	E_+^{3z}  $+i$ 
Site 2	A_1^{3xy} 	E_-^{3xy}  $-i$ 	E_+^{3xy}  $+i$ 
Site 3	A_2^{3xy} 	$E_-^{3xy'}$  $-i$ 	$E_+^{3xy'}$  $+i$ 

FIG. 2. Sketch of the symmetry-adapted basis of localized spins tabulated in Table II. The spin moments are colored-coded as in Fig. 1.

B. Selection rule for optical excitation of spin dynamics

In this section, we analyze the symmetry-adapted bases of the localized spins that are linearly coupled to the external field based on the symmetry. The circularly polarized external field is defined as

$$\mathbf{F}_\pm(t) = \frac{1}{\sqrt{2}}(1, \pm i, 0) \exp(-i\omega t),$$

where the minus sign ($-$) represents the CW mode and the plus sign ($+$) represents the CCW mode. Like in Table I, the external fields are classified in terms of irreducible representations and eigenvalues for operation 3_z . The results are shown in Table II. For instance, the eigenvalue of the clockwise rotatory field $\mathbf{F}_-(t)$ is ξ^- for operation 3_z , equal to that of the CW mode.

The symmetry indicates that we can excite the CW mode by the clockwise rotatory field $\mathbf{F}_-(t)$ and the CCW mode by the counterclockwise rotatory field $\mathbf{F}_+(t)$. The linearly polarized field F_x contains the clockwise and counterclockwise rotation fields and can excite both the CW and CCW modes. On the other hand, the eigenvalue of the magnetic field B_z is 1 for 3_z , which is the same as that of the AS mode. Thus, we can excite the AS mode by the magnetic field B_z along the z axis. In the following, we mainly delve into the linear responses to in-plane electric fields, and the AS modes play minor roles.

IV. LINEAR RESPONSE FUNCTIONS

In this section, we present the results of the real-time simulation of the spin-charge coupled system. First, we calculate the magnetic susceptibility of the symmetry-adapted bases of the localized spin system in Sec. IV A. Second,

TABLE II. Eigenvalues of the external field of localized spins under the symmetry operator of magnetic point group \mathcal{G} . The symmetry-adapted bases listed in the last column are linearly coupled to the external field in the row.

	3_z	$\theta 2_x$	Basis function
E^\pm	ξ^\pm	-1	$E_\pm^{1xy}, E_\pm^{3z}, E_\pm^{3xy}, E_\pm^{3xy'}$
B^\pm	ξ^\pm	$+1$	$E_\pm^{1xy}, E_\pm^{3z}, E_\pm^{3xy}, E_\pm^{3xy'}$
B^z	$+1$	$+1$	$A_1^{1z}, A_1^{3z}, A_1^{3xy}, A_2^{3xy}$

we calculate the linear optical conductivity of the electron system in Sec. IV B. Third, we calculate the electromagnetic susceptibility of the localized spin system in Sec. IV C. We also quantitatively evaluate the electromagnetic susceptibility of the collective modes.

A. Magnetic susceptibility

In this section, we show the magnetic susceptibility of the symmetry-adapted bases of the localized spins to corroborate the collective spin excitations in light of the frequency dependence. We calculate the magnetic susceptibility $\chi_{\alpha\mu}(\omega)$ written in the symmetry-adapted basis as

$$\Delta\tilde{\psi}_\alpha(\omega) = \chi_{\alpha\mu}(\omega)B_\mu(\omega), \quad (21)$$

where we defined the Fourier component of $\Delta\tilde{\psi}_\alpha(t) = \tilde{\psi}_\alpha(t) - \tilde{\psi}_\alpha(0)$, representing the modulation of localized spins in the symmetry-adapted representation. The response function $\chi_{\alpha\mu}(\omega)$ is obtained by taking the Gaussian magnetic field $\mathbf{F}(t) = \mathbf{B}(t)$ [Eq. (15)], which is coupled to the localized spins. The perturbation is expressed by the Hamiltonian

$$H_{\text{ext}}(t) = - \sum_a \mathbf{B}(t) \cdot \mathbf{S}_a. \quad (22)$$

The perturbation takes place without breaking the translation symmetry, and the time evolution can be traced in parallel between different momenta as in the case of the uniform vector potential [Eq. (6)].

We plot the magnetic susceptibilities of the symmetry-adapted bases belonging to the different symmetries in Fig. 3. In Fig. 3(a), the magnetic susceptibility $\chi_{\alpha z}$ with $\alpha = A_1^{1z}, A_1^{3z}, A_1^{3xy}, A_2^{3xy}$ (AS modes) is shown. Consistent with the symmetry analysis in Sec. III B, the out-of-plane magnetic field is coupled to the AS modes but makes no contribution to the CW and CCW modes. On the other hand, the CW and CCW modes respond to the in-plane magnetic fields as observed in the plots for $\chi_{\alpha x}$ in Figs. 3(b) and 3(c).

As a result, the spectrum of magnetic susceptibility is determined by three types of collective modes and consists of four peaks, that is, one for the AS modes, two for the CW mode, and one for the CCW mode. The number of collective modes is consistent with the analysis of the magnon spectrum [30], and the lowest-energy ($\omega \simeq 0.09$) peak comes from the magnon band whose gap energy at $\mathbf{k} = \mathbf{0}$ is due to the

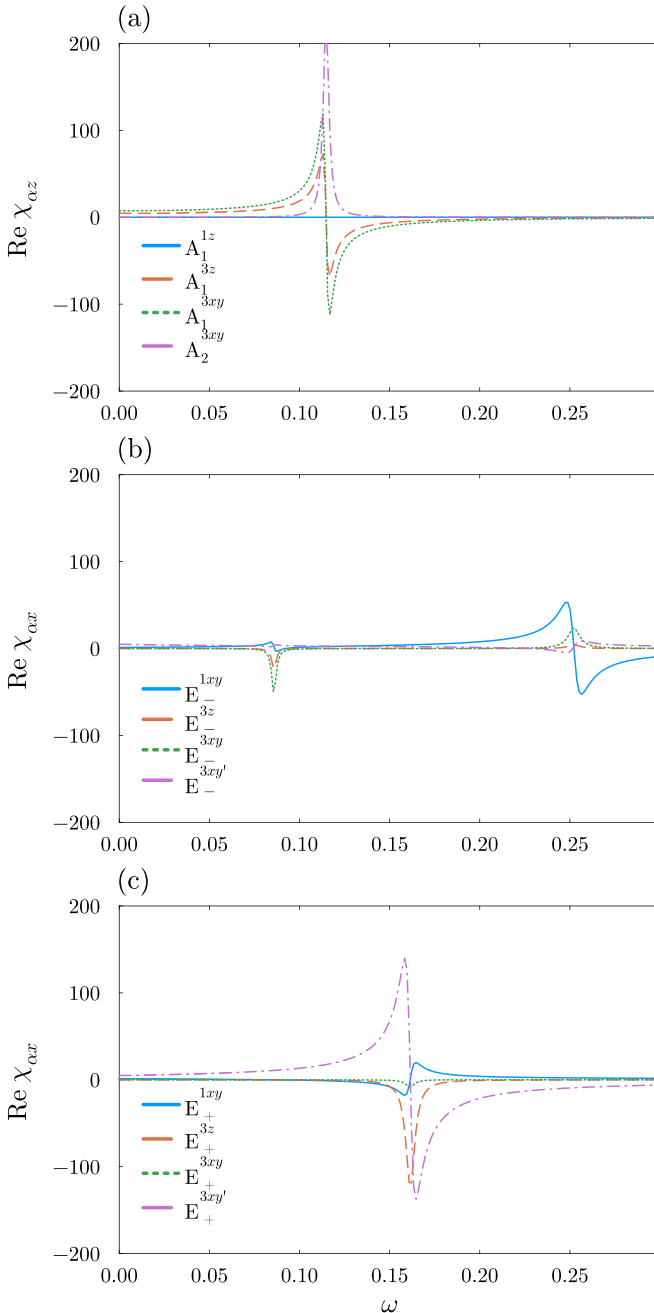


FIG. 3. (a) Linear magnetic susceptibility of the AS mode to the out-of-plane magnetic field. (b) Linear magnetic susceptibility of the CW mode to the magnetic field along the x axis. (c) Linear magnetic susceptibility of the CCW mode to the in-plane magnetic field.

magnetic anisotropy K_z in Eq. (1). We note that only the $\mathbf{k} = \mathbf{0}$ spin excitation is present since the system is perturbed by the uniform light field parametrized by $\mathbf{E}(t)$.

B. Optical conductivity

In this section, we investigate the linear optical conductivity. The linear optical conductivity is written as

$$j_\mu(\omega) = \sigma_{\mu\nu}(\omega)E_\nu(\omega), \quad (23)$$

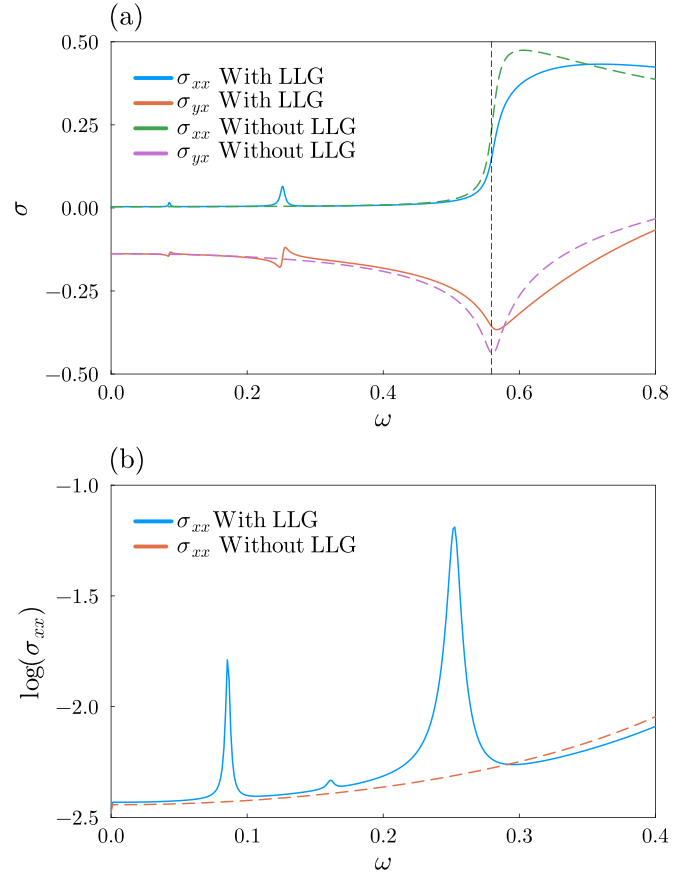


FIG. 4. (a) Linear optical conductivity of the system. The blue solid line and the green dashed line indicate the longitudinal optical conductivity with and without updating the spin configurations, respectively. The orange solid line and the purple dashed line indicate the transverse optical conductivity with and without updating the spin configurations, respectively. The black dashed line indicates the band gap frequency. (b) Longitudinal optical conductivity at log scale. The blue solid line and the orange dashed line indicate the calculation with and without updating the spin configurations.

where $\mu, \nu = x, y$ since the electronic Hamiltonian is built into the two-dimensional system. $j_\mu(\omega)$ is the Fourier component of the electric current in Eq. (14).

We plot the frequency dependence of the linear optical conductivity $\sigma_{\mu\nu}(\omega)$ in Fig. 4. The optical gap is at $\omega \simeq 0.55$ [vertical dashed line in Fig. 4(a)], indicating the insulating state of the adopted model. In Fig. 4(a), we show the longitudinal optical conductivity σ_{xx} and the transverse optical conductivity σ_{yx} . The solid lines (“With LLG”) represent the optical conductivity incorporating the effect of the localized spin dynamics following the LLG equation, while the dashed lines (“Without LLG”) represent the optical conductivity without the effect. In Fig. 4(b), we show the longitudinal optical conductivity σ_{xx} with and without the LLG simulation in log scale.

There are two consequences of spin dynamics on the optical conductivity. First, $\text{Re } \sigma(\omega)$ with the LLG simulation shows three resonance peaks in the in-gap regime, which are absent in the independent particle approximation. Due to the increased degrees of freedom of the local spins, more

optical conductivity peaks are observed in the in-gap regime than in Refs. [4,6]. The peaks at $\omega \simeq 0.09, 0.25$ correspond to CW modes, as inferred from the magnetic susceptibility [Fig. 3(b)], and the peak at $\omega \simeq 0.16$ is for CCW modes [see Fig. 3(c)]. The peak height for $\omega \simeq 0.16$ is much smaller than that at $\omega \simeq 0.09, 0.25$. The prominent difference can be understood from the electromagnetic susceptibility corroborated in Sec. IV C.

Second, the spin dynamics leads to the modification of the optical conductivity in the spectrum above the band gap as well as the in-gap optical excitations. This modification is also carried by the collective spin dynamics, while the localized spins are driven by the electronic spin excitations responding to the irradiating light. It is noteworthy that the in-gap and above-gap optical excitations are in a trade-off relationship due to the sum rule $\int \text{Re } \sigma_{\mu\nu}(\omega) d\omega = \text{const}$. In the spin-charge coupled system with the AIAO spin texture, the collective modes belonging to the different symmetries affect the optical conductivity. Therefore, we can selectively excite the collective modes which influence electronic transport.

C. Electromagnetic susceptibility

Our focus is on the richer collective spin excitations originating from the AIAO state and on their impact on the electric response, and thus, let us undertake more detailed investigations of the in-gap optical excitations by considering the electromagnetic susceptibility. The electromagnetic susceptibility $\kappa_{\alpha\mu}(\omega)$ of the symmetry-adapted form of the localized spin excitation ψ_α is written as

$$\Delta \tilde{\psi}_\alpha(\omega) = \kappa_{\alpha\mu}(\omega) E_\mu(\omega). \quad (24)$$

We plot the spectrum of the electromagnetic susceptibility $\kappa_{\alpha x}$ with the electric field $\mathbf{E} \parallel \hat{x}$ in Fig. 5. Owing to the selection rule tabulated in Table II, only the CW and CCW modes contribute to the electromagnetic susceptibility $\kappa_{\alpha x}$. Then, we show the electromagnetic susceptibility relevant to the CW modes [Fig. 5(a)] and CCW modes [Fig. 5(b)]. The electromagnetic susceptibility of the CCW mode is much smaller than that of the CW mode.

The in-gap peaks of the optical conductivity are caused by resonant excitation of collective spin dynamics, and thus, peak amplitude implies the electrical activity of each collective excitation. For instance, the electrical activity of the CCW mode is small, as observed in the electromagnetic susceptibility plotted in Fig. 5(b), leading to the negligibly small peak in the optical conductivity spectrum [Fig. 4(b)]. More specifically, the mechanism of electric-active collective spins dynamics is as follows: first, the electric field coupled to the electron system stimulates the magnetization response of electrons' spins through the spin-orbit coupling [third term in Eq. (1)]. Then, the perturbed spin moment of electrons induces the dynamics of the localized spins as a consequence of the exchange interaction between them [second term in Eq. (1)]. The resultant coupling between the electric field and the localized spins indicates the electromagnetic response denoted by Eq. (24).

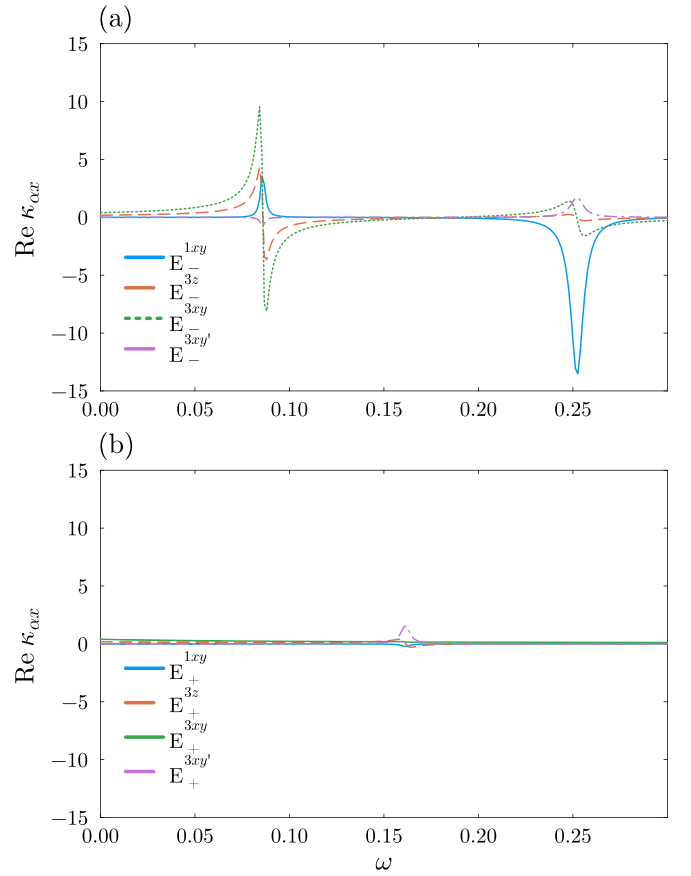


FIG. 5. Linear electromagnetic susceptibility $\kappa_{\alpha x}$. The symmetry-adapted basis ψ_α is taken from (a) the CW modes and (b) the CCW modes.

The mechanism can be formulated by decomposing the electromagnetic susceptibility into two parts as

$$\kappa_{\alpha x}(\omega) = \sum_{\beta} \chi_{\alpha\beta}^S(\omega) \kappa_{\beta x}^\sigma(\omega) \quad (25)$$

$$\equiv \sum_{\beta} \kappa_{\alpha\beta x}(\omega). \quad (26)$$

$\kappa_{\beta x}^\sigma(\omega)$ is the bare electromagnetic susceptibility, indicating the correlation between the electric field is

$$\sum_{\mu} c_a^\mu(\alpha) \Delta \langle \sigma_a^\mu \rangle(\omega) = \kappa_{\alpha v}^\sigma(\omega) E_v(\omega), \quad (27)$$

where we define the Fourier component of $\Delta \langle \sigma_a^\mu \rangle(t) = \langle \sigma_a^\mu \rangle(t) - \langle \sigma_a^\mu \rangle(0)$, representing the modulation of itinerant spins in the symmetry-adapted representation. This susceptibility does not include the dynamical effects of the localized spins, so we calculate $\kappa_{\alpha x}^\sigma(\omega)$ by the real-time simulation without updating the local spin moments.

We also define $\chi_{\alpha\beta}^S(\omega)$, which is the magnetic susceptibility denoting the correlation between the symmetry-adapted modes (ψ_α, ψ_β). Based on the symmetry, $\chi_{\alpha\beta}^S(\omega)$ is finite when the symmetry-adapted bases α and β belong to the same mode. The response function $\chi_{\alpha\beta}^S(\omega)$ is obtained by taking the Gaussian magnetic field, which is proportional to the symmetry-adapted basis ψ_β . The perturbation is expressed

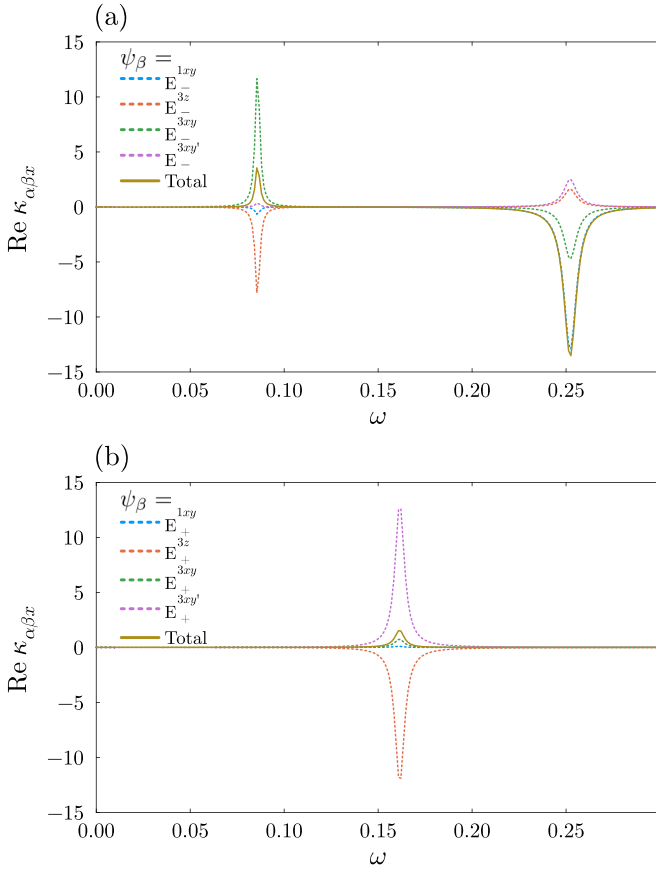


FIG. 6. (a) The decomposition of the electromagnetic susceptibility of the collective mode $\psi_\alpha = E_-^{1xy}$. (b) The decomposition of the electromagnetic susceptibility of the collective mode $\psi_\alpha = E_+^{3xy'}$.

by the Hamiltonian

$$H_{\text{ext}}^\beta(t) = -J \sum_{\alpha\mu} \frac{B_0}{\sqrt{2\pi\sigma^2}} \exp\left(-\frac{(t-t_0)^2}{2\sigma^2}\right) c_a^\mu(\beta) S_a^\mu, \quad (28)$$

where B_0 is the amplitude of the Gaussian magnetic field.

Combining $\chi_{\alpha\beta}^S(\omega)$ and $\kappa_{\alpha\beta x}^\sigma(\omega)$, we can calculate the decomposed component $\kappa_{\alpha\beta x}(\omega)$. As a result, the electromagnetic susceptibility $\kappa_{\alpha\mu}(\omega)$ of the collective mode ψ_α is determined by the interference of $\kappa_{\alpha\beta\mu}(\omega)$ with respect to the mediating modes labeled by β .

Taking the CW E_-^{1xy} and CCW $E_+^{3xy'}$ modes for ψ_α in Eq. (26), we plot the decomposed electromagnetic susceptibility in Fig. 6. In the case of $\psi_\alpha = E_-^{1xy}$, for example, the localized spin response to the electric field is mediated by the fluctuations denoted by $\sum_\mu c_a^\mu(\beta) \langle \sigma_a^\mu \rangle$, which are symmetry adapted to the CW modes (E_-^{1xy} , E_-^{3z} , E_-^{3xy} , and $E_-^{3xy'}$). Similarly, the electromagnetic susceptibility of the collective mode $E_+^{3xy'}$ is mediated by those with the same symmetry as the CCW modes of localized spins.

As for the electromagnetic susceptibility of the CW mode, the interference of the mediating spin fluctuations results in a sizable electromagnetic susceptibility for $\psi_\alpha = E_-^{1xy}$. On the other hand, while each $\kappa_{\alpha\beta x}$ makes a significant contribution, destructive interference is observed in the case of the CCW mode, giving rise to a much smaller electromagnetic suscep-

tibility in total. These results imply that the CCW modes are less electrically active when compared to the CW modes and hence offer negligible optical conductivity [peak around $\omega \simeq 0.16$ in Fig. 4(b)]. The constructive and destructive interference effects are features unique to the system hosting the complex spin texture, and their identification has been accomplished with the developed efficient computational method for the real-time evolution of the spin-charge coupled system.

V. SUMMARY

In this study, we developed an efficient real-time simulation of the spin-charge coupled system and applied this method to a two-dimensional system with a complex spin texture. We investigated how the collective excitation of the localized spins influences the optical response of the electronic system. First, we identified the symmetry-adapted bases of the localized spins and further classified them with circular polarization. This allowed us to clarify the reaction of the collective modes of the localized spins to external stimuli. Next, we calculated the linear response functions of the spin-charge coupled system. The magnetic susceptibility is conveniently decomposed by the symmetry-adapted bases and is determined by the resonant dynamics of the localized spins when the frequency of magnetic fields is in the in-gap regime. The observed collective modes have features similar to those of the skyrmionic system, implying the AIAO state is the minimum unit of the magnetic skyrmion.

The impact of the real-time simulation was demonstrated by the calculations of the linear optical conductivity, including the effect of the localized spins dynamics. The electrical activity of the collective spin motion results in the modification of the spectrum of optical conductivity such as in-gap peak structures. The collective modes differ in their influence on the optical conductivity; the rotatory modes of the localized spins affect the optical conductivity, but the AS mode of the localized spins does not affect the optical conductivity in the two-dimensional system. Finally, we discussed electromagnetic susceptibility, paying special attention to spin dynamics induced by light whose frequency is below the band gap. The electromagnetic susceptibilities of the CW and CCW modes were elucidated by decomposition into the bare electromagnetic susceptibility and magnetic susceptibility. As a result, the interference effect plays a key role in determining the contrasting electrical activity of the CW and CCW modes.

To conclude, we systematically investigated the spin-charge coupling by real-time simulations of the system with the AIAO magnetic order, which is considered the minimal unit of a magnetic skyrmion. The diverse collective excitations arising from the magnetic structure lead to multiple peak structures in the optical conductivity spectrum and exhibit different electrical activities due to interference effects between spin fluctuations. The essential ingredient is the optically active collective spin dynamics in the gapped system. Therefore, searching for a real material should be in the realm of inversion symmetry broken semiconductors or insulators with optically active magnons, such as GaV_4S_8 [35,36] and Cu_2OSeO_3 [37,38].

ACKNOWLEDGMENTS

This work is supported by Grants-in-Aid for Scientific Research from JSPS, KAKENHI, Grants No. JP23K13058 (H.W.), No. 22H00290 (T.N.), No. 24K00581 (T.N.), No. 21H04990 (R.A.), No. JP21H04437 (R.A.), and No. 19H05825 (R.A.); JST-PRESTO Grant No. JPMJPR20L7 (T.N.); JST-CREST Grants No. JPMJCR18T3 and No. JP-

MJCR23O4 (R.A.); JST-ASPIRE Grant No. JPMJAP2317 (R.A.); and JST-Mirai Grant No. JPMJMI20A1 (R.A.). K.H. was supported by the Program for Leading Graduate Schools (MERIT-WINGS). This work was supported by the RIKEN TRIP initiative (RIKEN Quantum, Advanced General Intelligence for Science Program, Multi-Electron Group).

- [1] M. Sotome, M. Nakamura, T. Morimoto, Y. Zhang, G.-Y. Guo, M. Kawasaki, N. Nagaosa, Y. Tokura, and N. Ogawa, *Phys. Rev. B* **103**, L241111 (2021).
- [2] T. Morimoto and N. Nagaosa, *Phys. Rev. B* **94**, 035117 (2016).
- [3] Y. Okamura, T. Morimoto, N. Ogawa, Y. Kaneko, G.-Y. Guo, M. Nakamura, M. Kawasaki, N. Nagaosa, Y. Tokura, and Y. Takahashi, *Proc. Natl. Acad. Sci. USA* **119**, e2122313119 (2022).
- [4] J. Iguchi, H. Watanabe, Y. Murakami, T. Nomoto, and R. Arita, *Phys. Rev. B* **109**, 064407 (2024).
- [5] Y. Murakami, D. Golež, T. Kaneko, A. Koga, A. J. Millis, and P. Werner, *Phys. Rev. B* **101**, 195118 (2020).
- [6] T. Kaneko, Z. Sun, Y. Murakami, D. Golež, and A. J. Millis, *Phys. Rev. Lett.* **127**, 127402 (2021).
- [7] A. Ono and S. Ishihara, *npj Comput. Mater.* **7**, 171 (2021).
- [8] K. Ohgushi, S. Murakami, and N. Nagaosa, *Phys. Rev. B* **62**, R6065 (2000).
- [9] I. Martin and C. D. Batista, *Phys. Rev. Lett.* **101**, 156402 (2008).
- [10] N. Nagaosa and Y. Tokura, *Phys. Scr.* **T146**, 014020 (2012).
- [11] N. Nagaosa and Y. Tokura, *Nat. Nanotechnol.* **8**, 899 (2013).
- [12] S. Mühlbauer, B. Binz, F. Jonietz, C. Pfleiderer, A. Rosch, A. Neubauer, R. Georgii, and P. Böni, *Science* **323**, 915 (2009).
- [13] T. Kurumaji, T. Nakajima, M. Hirschberger, A. Kikkawa, Y. Yamasaki, H. Sagayama, H. Nakao, Y. Taguchi, T. Arima, and Y. Tokura, *Science* **365**, 914 (2019).
- [14] M. Hirschberger, T. Nakajima, S. Gao, L. Peng, A. Kikkawa, T. Kurumaji, M. Kriener, Y. Yamasaki, H. Sagayama, H. Nakao, K. Ohishi, K. Kakurai, Y. Taguchi, X. Yu, T.-H. Arima, and Y. Tokura, *Nat. Commun.* **10**, 5831 (2019).
- [15] Y. Akagi and Y. Motome, *J. Phys. Soc. Jpn.* **79**, 083711 (2010).
- [16] K. Hamamoto, M. Ezawa, and N. Nagaosa, *Phys. Rev. B* **92**, 115417 (2015).
- [17] A. Matsui, T. Nomoto, and R. Arita, *Phys. Rev. B* **104**, 174432 (2021).
- [18] W. Feng, J.-P. Hanke, X. Zhou, G.-Y. Guo, S. Blügel, Y. Mokrousov, and Y. Yao, *Nat. Commun.* **11**, 118 (2020).
- [19] J. Zhou, Q.-F. Liang, H. Weng, Y. B. Chen, S.-H. Yao, Y.-F. Chen, J. Dong, and G.-Y. Guo, *Phys. Rev. Lett.* **116**, 256601 (2016).
- [20] P. Park, W. Cho, C. Kim, Y. An, Y.-G. Kang, M. Avdeev, R. Sibille, K. Iida, R. Kajimoto, K. H. Lee, W. Ju, E.-J. Cho, H.-J. Noh, M. J. Han, S.-S. Zhang, C. D. Batista, and J.-G. Park, *Nat. Commun.* **14**, 8346 (2023).
- [21] H. Takagi, R. Takagi, S. Minami, T. Nomoto, K. Ohishi, M.-T. Suzuki, Y. Yanagi, M. Hirayama, N. D. Khanh, K. Karube, H. Saito, D. Hashizume, R. Kiyonagi, Y. Tokura, R. Arita, T. Nakajima, and S. Seki, *Nat. Phys.* **19**, 961 (2023).
- [22] N. J. Ghimire, A. S. Botana, J. S. Jiang, J. Zhang, Y.-S. Chen, and J. F. Mitchell, *Nat. Commun.* **9**, 3280 (2018).
- [23] N. D. Khanh, T. Nakajima, X. Yu, S. Gao, K. Shibata, M. Hirschberger, Y. Yamasaki, H. Sagayama, H. Nakao, L. Peng, K. Nakajima, R. Takagi, T.-H. Arima, Y. Tokura, and S. Seki, *Nat. Nanotechnol.* **15**, 444 (2020).
- [24] M. Mochizuki, *Phys. Rev. Lett.* **108**, 017601 (2012).
- [25] M. Mruczkiewicz, M. Krawczyk, and K. Y. Guslienko, *Phys. Rev. B* **95**, 094414 (2017).
- [26] M. Mruczkiewicz, P. Gruszecki, M. Zelent, and M. Krawczyk, *Phys. Rev. B* **93**, 174429 (2016).
- [27] S. Seki, M. Garst, J. Waizner, R. Takagi, N. D. Khanh, Y. Okamura, K. Kondou, F. Kagawa, Y. Otani, and Y. Tokura, *Nat. Commun.* **11**, 256 (2020).
- [28] Y. Onose, Y. Okamura, S. Seki, S. Ishiwata, and Y. Tokura, *Phys. Rev. Lett.* **109**, 037603 (2012).
- [29] Y. Okamura, F. Kagawa, M. Mochizuki, M. Kubota, S. Seki, S. Ishiwata, M. Kawasaki, Y. Onose, and Y. Tokura, *Nat. Commun.* **4**, 2391 (2013).
- [30] Y. Akagi, M. Udagawa, and Y. Motome, *J. Phys. Soc. Jpn.* **82**, 123709 (2013).
- [31] S. Hayami, R. Ozawa, and Y. Motome, *Phys. Rev. B* **95**, 224424 (2017).
- [32] L. Yue and M. B. Gaarde, *J. Opt. Soc. Am. B* **39**, 535 (2022).
- [33] G. B. Ventura, D. J. Passos, J. M. B. Lopes dos Santos, J. M. Viana Parente Lopes, and N. M. R. Peres, *Phys. Rev. B* **96**, 035431 (2017).
- [34] Y. Murakami and M. Schüler, *Phys. Rev. B* **106**, 035204 (2022).
- [35] P. Padmanabhan, F. Sekiguchi, R. B. Versteeg, E. Slivina, V. Tsurkan, S. Bordács, I. Kézsmárki, and P. H. M. van Loosdrecht, *Phys. Rev. Lett.* **122**, 107203 (2019).
- [36] I. Kézsmárki, S. Bordács, P. Milde, E. Neuber, L. M. Eng, J. S. White, H. M. Rønnow, C. D. Dewhurst, M. Mochizuki, K. Yanai, H. Nakamura, D. Ehlers, V. Tsurkan, and A. Loidl, *Nat. Mater.* **14**, 1116 (2015).
- [37] S. Seki, X. Z. Yu, S. Ishiwata, and Y. Tokura, *Science* **336**, 198 (2012).
- [38] J. S. White, K. Prša, P. Huang, A. A. Omrani, I. Živković, M. Bartkowiak, H. Berger, A. Magrez, J. L. Gavilano, G. Nagy, J. Zang, and H. M. Rønnow, *Phys. Rev. Lett.* **113**, 107203 (2014).